Pterodactyl: The Development and Performance of Guidance Algorithms for a Mechanically Deployed Entry Vehicle

Breanna J. Johnson[1], Daniela Rocca-Bejar[2]
NASA Johnson Space Center, Houston, TX, 77058

Ping Lu[3]
San Diego State University, San Diego, CA 92182

Ben E. Nikaido[4], Bryan C. Yount[5], and Sarah N. D'Souza[6]
NASA Ames Research Center, Mountain View, CA

Zane Hays[7]
AMA, Inc., Moffet Field, CA, 94035

Pterodactyl is a NASA Space Technology Mission Directorate (STMD) project focused on developing a design capability for optimal, scalable, Guidance and Control (G&C) solutions that enable precision targeting for Deployable Entry Vehicles (DEVs). This feasibility study is unique in that it focuses on the rapid integration of targeting performance analysis with structural & packaging analysis, which is especially challenging for new vehicle and mission designs. This paper will detail the guidance development and trajectory design process for a lunar return mission, selected to stress the vehicle designs and encourage future scalability. For the five G&C configurations considered, the Fully Numerical Predictor-Corrector Entry Guidance (FNPEG) was selected for configurations requiring bank angle guidance and FNPEG with Uncoupled Range Control (URC) was developed for configurations requiring angle of attack and sideslip angle guidance. Successful G&C configurations are defined as those that can deliver payloads to the intended descent and landing initiation point, while abiding by trajectory constraints for nominal and dispersed trajectories.

I. Nomenclature

C_A , C_Y , C_N	=	aerodynamic axial, side, and normal force coefficients
C_D , C_S , C_L	=	aerodynamic drag, side, and lift force coefficients
D, S, L	=	aerodynamic drag, side, and lift forces
α	=	angle of attack
β	=	sideslip angle
σ	=	bank angle
e	=	energy (negated specific mechanical energy from orbital mechanics)
r	=	planetocentric radial distance
V	=	planet-relative velocity
g	=	gravitational acceleration
s	=	great-circle range to target site
z	=	error of the range to target
k	=	number of predictor corrector iterations
λ	=	step size used in Gauss-Newton update

[1] Aerospace Engineer, Flight Mechanics and Trajectory Design Branch NASA JSC/EG5.
[2] Aerospace Engineer Trainee, Flight Mechanics and Trajectory Design Branch NASA JSC/EG5.
[3] Professor and Chair, Department of Aerospace Engineering; plu@sdsu.edu, Fellow AIAA.
[4] Aerospace Flight Systems Engineer, Systems Analysis Office, NASA ARC/AA.
[5] Experimental Facility Developer, Engineering Systems Division, NASA ARC/RE.
[6] Principal Investigator, Systems Analysis Office, NASA ARC/AA.
[7] Aerospace Engineer, Analytical Mechanics Associates, Inc.

γ	=	planetocentric flight path angle of the planet-relative velocity
θ	=	longitude
ϕ	=	planetocentric latitude
ψ	=	planetocentric azimuth of the planet-relative velocity
m	=	vehicle mass
Ω	=	spherical planet rotation rate
ρ	=	ratio of the sensed to nominal aerodynamic force used in the fading memory filter
η	=	scaling factor for the aerodynamic fading memory filter
X, Y, Z	=	aerodynamic polynomial fit coefficients
M	=	Mach
A	=	aerodynamic reference area
Γ	=	conversion factor from aerodynamic acceleration to coefficient
K	=	lateral control logic gain
q	=	dynamic pressure
c	=	proportional gain tuning and scaling parameter for sideslip angle
ω	=	lateral control logic desired frequency
ξ	=	lateral control logic desired damping ratio

II. Introduction

ENTRY, descent, and landing (EDL) has been identified as a core area of investment in NASA's Strategic Technology Investment Plan (NASA STIP). STIP lists the space technologies needed to help achieve NASA's science, technology, and exploration goals across the agency. Within the EDL core area, deployable hypersonic decelerators, also known as deployable entry vehicles (DEVs), have been identified as an area of investment, due to their potential to revolutionize payload delivery methods to Earth and other planets. These vehicles, which can deploy their heat shields or alter their shape before entry, exploit an increased and more effective drag ratio by using less mass than traditional blunt body vehicles with rigid aeroshells. DEVs like Adaptive Deployable Entry and Placement Technology (ADEPT) and Hypersonic Inflatable Aerodynamic Decelerator (HIAD) have demonstrated the capability of transporting the equivalent science payloads of blunt body rigid aeroshells, while using a significantly smaller diameter when stowed within a launch vehicle [1, 2]. While DEVs' increased energy dissipation for less mass is an attractive feature, their ability to contract and expand would require advancements in the current state-of-the-art guidance and control (G&C) architectures used by traditional rigid vehicles. Pterodactyl, a project funded by NASA's Space Technology Mission Directorate (STMD), aims to provide feasible integrated G&C solutions for DEVs, complete with optimized vehicle designs and packaging analyses.

The Lifting Nano-ADEPT (LNA) vehicle is chosen as the DEV to demonstrate the integrated G&C solutions [3]. Three candidate control systems are explored in this study to determine the most feasible and robust option. Figure 1 shows the baseline configuration (no entry control system), the Reaction Control System (RCS) configuration, the aerosurfaces (flaps) configuration, and the mass movement configuration. It should be noted that each configuration would have an RCS system for the exo-atmospheric Moon to Earth trajectory course corrections, but only the RCS configuration would use that system for control during hypersonic entry. Early structural and aerodynamic analyses for the integrated vehicle configurations suggested a need for a bank angle guidance algorithm, the heritage guidance approach used in many hypersonic entry precision targeting vehicles, as well as an additional need for the development of a non-bank angle guidance. For this reason, Pterodactyl considered five different G&C configurations during its design phase:

1. RCS for bank angle control
2. Flaps control system for bank angle control
3. Flaps control system for angle of attack and sideslip angle control
4. Mass Movement control system for bank angle control
5. Mass Movement control system for angle of attack and sideslip angle control

The development of an angle of attack (α, alpha) and sideslip angle (β, beta) guidance was chosen to decouple the downrange and crossrange control into two separate control channels, exploiting the expected pitch and yaw capabilities of the flaps and mass movement control system options. This paper will discuss the strengths of each

guidance methodology, the insights gained from trajectory design maps, the challenges of closing a fully integrated design, and the robustness of each explored configuration.

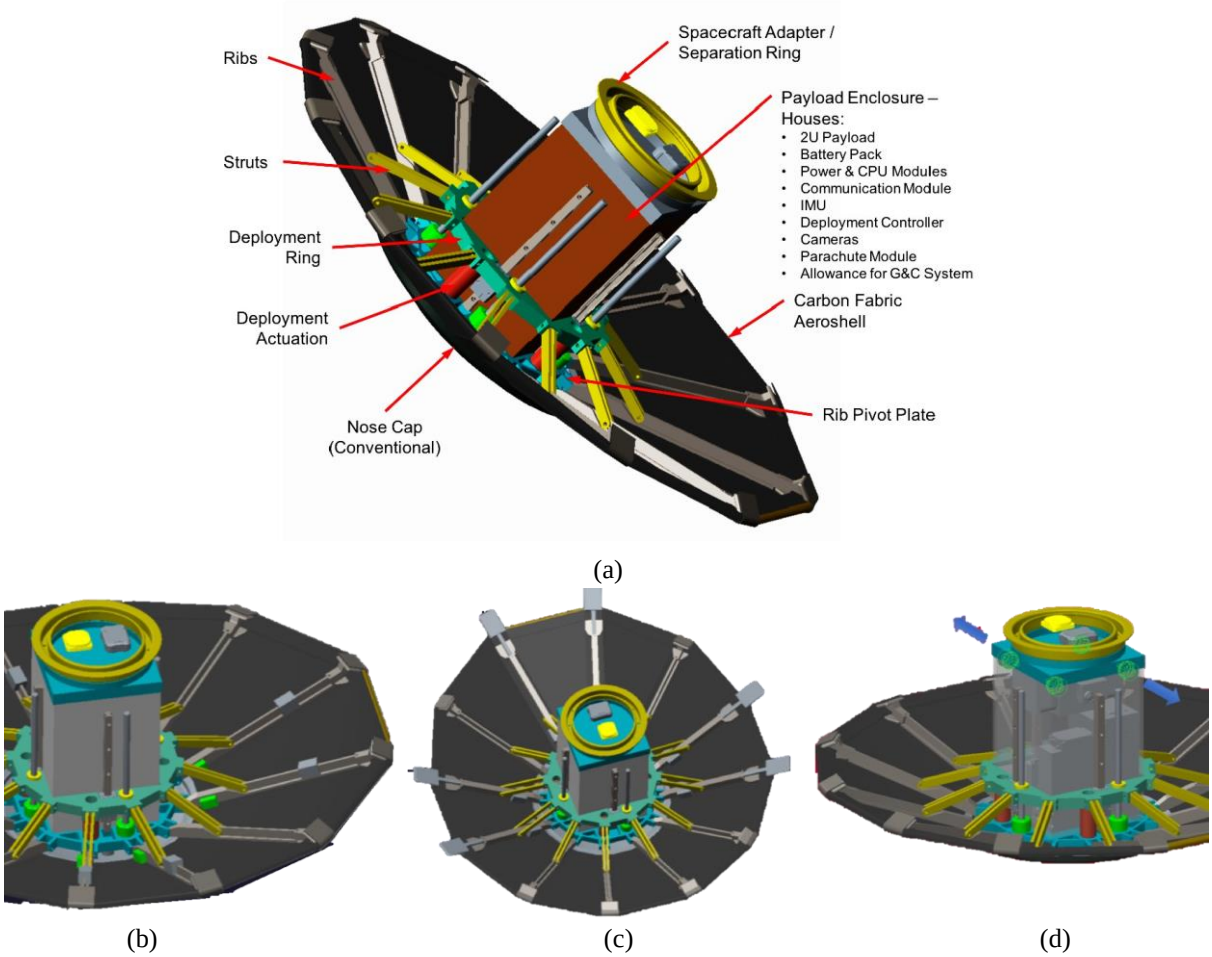

Fig. 1 Lifting Nano-ADEPT baseline and control system configurations: (a) Baseline; (b) Mass movement; (c) Flaps; (d) RCS.

III. Guidance Methodology

Recent advances in the field of hypersonic entry guidance has resulted in a new class of algorithms with the capability to adapt to large trajectory dispersions without the need for a pre-planned reference trajectory. In flight, these guidances rely on numerical predictor correctors that internally predict a new trajectory at each guidance step, then correct that trajectory based on predicted and targeted final conditions. If a skip entry is desired, algorithms reliant on numerical predictor correctors can especially provide improvements over traditional entry guidances that are reliant on tracking laws [4]. Due to the rapid design and development cycle needed by the Pterodactyl project, the use of a numerical predictor corrector entry guidance algorithm became the clear choice.

Early in the development, it was found that the iterative integration of the vehicle's control system with its design and packaging constraints could cause significant changes in lift-to-drag ratio (L/D), mass, and aerodynamic characteristics. For these reasons, in addition to its unique need of little gain tuning between different vehicle and mission ConOps inputs, the Fully Numerical Predictor-corrector Entry Guidance (FNPEG) was selected as the bank angle guidance algorithm. Unlike other guidance algorithms, FNPEG is a unified method based on the same algorithmic principles applicable to a wide range of vehicles, from low to high L/D. FNPEG may be applied to skip as well as direct entry for orbital and sub-orbital entry missions using the same unifying equations of motion, essentially eliminating the need for complicated transition logic between direct and skip phases of entry. FNPEG has been tested and evaluated at Johnson Space Center in the Orion simulation environment, Advanced NASA Technology Architecture for Exploration Studies (ANTARES), as well as in the Flight Analysis Simulation Tool

(FAST) [5, 6]. The algorithm has also been shown to compare favorably with the Orion entry guidance algorithm PredGuid, have strong convergence rates, and be able to enforce complicated (quadratic) inequality heating and aerodynamic load constraints.

Typically, a low L/D entry vehicle must employ actuators that primarily provide roll control, such that the vehicle may roll about the velocity vector, pointing the lift vector in the direction of guided bank commands. However, the Pterodactyl project is challenged to provide precision targeting for control systems that may be weaker in controlling the body's roll axis than its pitch and yaw axes. Figure 2 shows the rotations about these body frame axes for the LNA, where TE denotes the trailing edge that points nadir during flight and LE denotes the leading edge. When the angle of attack is negative, as shown, the vehicle flies with positive lift in the zenith direction.

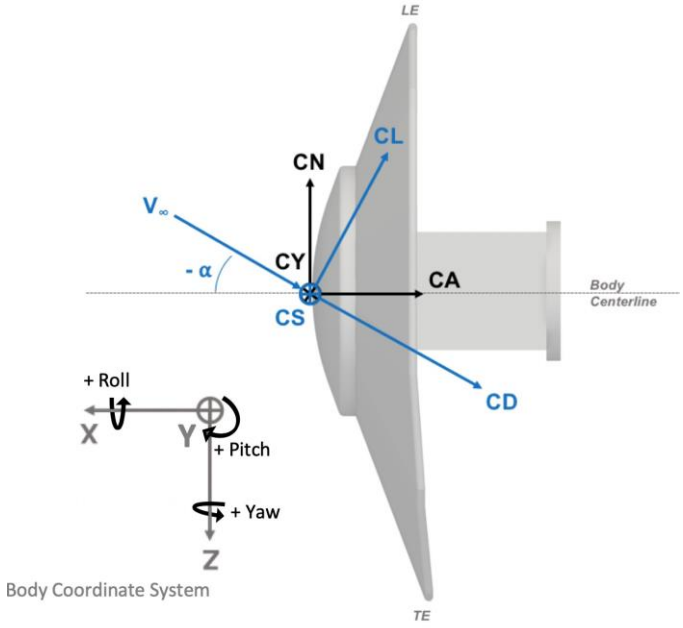

Fig. 2 Pterodactyl coordinate frames and aerodynamic coefficients.

Leveraging the aforementioned strengths of FNPEG, this paper introduces a new guidance algorithm, FNPEG with Uncoupled Range Control (FNPEG URC), to provide guided commands for vehicles with stronger pitch-yaw control authority than roll. For each guidance cycle, FNPEG outputs a bank angle command, assuming a fixed alpha profile provided by the user, whereas FNPEG URC outputs an alpha and beta command, assuming a fixed bank angle is maintained throughout flight. FNPEG URC, like FNPEG, uses the Gauss-Newton method within the predictor-corrector logic to search for the best command angle magnitude vs. energy profile resulting in minimal miss distance, where the energy-like variable e is defined as

$$e = \frac{V^2}{2} - \frac{\mu}{r} \tag{1}$$

and the alpha-magnitude profile is defined as

$$|\alpha(e)| = \alpha_0 + \frac{FGF^H}{F_I GF_H}(\alpha_1 - \alpha_0) \tag{2}$$

In Equation 1, V is the planet-relative velocity and r is the planetocentric radial distance to the vehicle. The alpha-magnitude profile, like FNPEG's bank angle magnitude profile, is parameterized by a linear function of e. In order to reserve sufficient energy margin at the end of the trajectory for heavily dispersed Monte Carlo cases, FNPEG's bank vs. energy profile becomes more lift up (defined by $\sigma = 0°$) as the trajectory nears the target. However, to keep these reserve margins for FNPEG URC, the alpha vs. energy profile must increase the magnitude of lift by increasing the magnitude of the alpha command as the trajectory nears the target. Figure 3 shows the mirrored linear profiles for FNPEG and FNPEG URC.

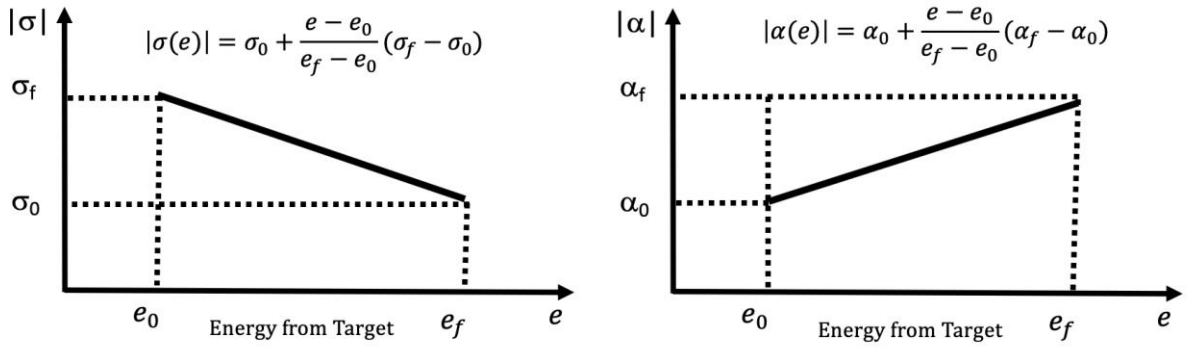

Fig. 3 FNPEG and FNPEG URC linear command angle vs. energy profiles.

To retain the strong convergence reliability from FNPEG, FNPEG URC's numerical method solves a least-squares problem with a single univariate function to find the α_D needed to minimize the error function defined as

$$f(\alpha_D) = \frac{:0s}{?}\ \mathrm{PQRQ}\ Se\ \mathrm{TU}^{?} \tag{3}$$

where s_{PQRQ} defines the great-circle range to the target site. Within each prediction-correction cycle, the calculated α_D and current e_D are used to predict the resultant trajectory by numerically integrating the entry hypersonic equations of motion. If the calculated α_D does not meet the terminal constraint on the error (z) of the range to target (s_J^*) from Equation 4, then the step-size (λ_W) controlled Gauss-Newton update in Equation 5 will correct the trajectory solution by updating to a new α_D for each k iteration.

$$z(\alpha_D) = sSe_J\mathrm{T} - s^*_J \tag{4}$$

$$\alpha^{WX:}_D = \alpha^W_D - \lambda_W \frac{\mathrm{YJSZ_H^[T/YZ_H^>}}{\mathrm{0YJSZ_H^[T/YZ_H\,U}} = \alpha^W_D - \lambda_W \frac{\mathrm{JSZ_H^[T}}{\mathrm{YJSZ_H^[T/YZ_H}} \tag{5}$$

Equation 5 highlights that this for this implementation of the Gauss-Newton method, we get the same equation that is used in the Newton-Raphson method. The Newton-Raphson method typically has higher convergence than many other Gauss-Newton cases due to its local superlinear or quadratic convergence [4]. It has been observed that like FNPEG, FNPEG URC has fast and reliable convergence rates based on these assumptions. If a solution is not found to satisfy the terminal constraint, the predictor corrector still outputs the α_D resulting in the smallest miss distance possible.

Fundamentally, FNPEG and FNPEG URC rely on many of the same assumptions for the equations of motion. Assumptions include a spherical rotating planet with constant rotation rate (Ω), no winds, and a simple planetocentric gravity model. Thus, the kinematic relations from FNPEG, shown in Equations 6-8, still apply

$$\dot{r} = V\sin\gamma \tag{6}$$

$$\theta = \frac{=\mathrm{cQde\ dfgh}}{;\mathrm{cQd\,i}} \tag{7}$$

$$\dot{\phi} = \frac{=\mathrm{jkl\ e\ jkl\ h}}{;} \tag{8}$$

where θ is the vehicle's longitude, ϕ is the vehicle's planetocentric latitude, γ is the planetocentric flight path angle of the planet-relative velocity, and ψ is the planetocentric azimuth of the planet-relative velocity defined clockwise from North at $\psi = 0°$. However, the dynamic relations from FNPEG would gain a side force term in trajectories using large angles of beta and side force. Upon rederivation using a similar methodology from Ref. 7, the dynamic equations are shown in Equations 9-11

$$\begin{aligned} V &= -\frac{\mathrm{m}}{\mathrm{n}} - g\sin\gamma + \Omega^{?}r\cos\phi\,(\sin\gamma\cos\phi - \cos\gamma\sin\phi\cos\psi) \\ \dot{\gamma} &= \frac{1}{V}\left[\frac{L}{m}\cos\sigma - \frac{S}{m}\sin\sigma - g\cos\gamma + \frac{V^{?}}{r}\cos\gamma + 2\Omega V\cos\phi\sin\psi\right. \end{aligned} \tag{9}$$

$$+\Omega^{?}r\cos\phi\,(\cos\gamma\cos\phi+\sin\gamma\sin\phi\cos\psi)] \tag{10}$$

$$\psi=\frac{1}{V}[\frac{L}{m}\frac{\sin\sigma}{\cos\gamma}+\frac{S}{m}\frac{\cos\sigma}{\cos\gamma}-\frac{V^{?}}{r}\cos\gamma\sin\psi\,tan\phi+2\Omega V(\tan\gamma\,cos\phi\cos\psi-sin\phi)$$

$$-\frac{\mathbf{j}^{>}}{\mathrm{jkl\ e}}\sin\phi\cos\phi\sin\psi \tag{11}$$

where m is the point mass of the vehicle, D is the aerodynamic drag force, L is the aerodynamic lift force, S is the aerodynamic side force, and g is the gravitational acceleration. As expected, from these general equations, we may recover the hypersonic equations of motion used in FNPEG when the side force is zero.

Like FNPEG, FNPEG URC uses first order fading memory filters to estimate the ratios of sensed to expected lift and drag ratios within the predictor corrector. Sensed aerodynamic accelerations would come from navigation sensor data in a flight, while the expected values come from the nominal alpha vs. Mach profiles. The scaling factor for the three axes are shown in Equations 12-14

$$\rho_{\mathrm{A}}^{\mathrm{gX:}}=\rho_{\mathrm{A}}^{\mathrm{g}}+(1-\eta)(\rho_{\mathrm{A}}-\rho_{\mathrm{A}}^{\mathrm{g}})\quad,\qquad 0<\eta<1 \tag{12}$$

$$\rho_{\mathrm{m}}^{\mathrm{gX:}}=\rho_{\mathrm{m}}^{\mathrm{g}}+(1-\eta)(\rho_{\mathrm{m}}-\rho_{\mathrm{m}}^{\mathrm{g}})\quad,\qquad 0<\eta<1 \tag{13}$$

$$\rho_{\mathrm{N}}^{\mathrm{gX:}}=\rho_{\mathrm{N}}^{\mathrm{g}}+(1-\eta)(\rho_{\mathrm{N}}-\rho_{\mathrm{N}}^{\mathrm{g}})\quad,\qquad 0<\eta<1 \tag{14}$$

where ρ represents the ratio of sensed to expected force, η represents the scaling factor, and n represents each guidance cycle [8]. This filter is very effective at reducing the effects of both aerodynamic as well as atmospheric uncertainty.

One of the great challenges in implementing alpha-beta guidance stems from difficulty in finding the estimated aerodynamic coefficients for lift (C_L), drag (C_D), and side force (C_S) efficiently in each predictor corrector iteration. With FNPEG, one equation could easily define the alpha - Mach number (M) relationship for C_{A} or C_{m} when beta is assumed constant. However, with FNPEG URC, each commanded alpha and beta fundamentally alter the values of these coefficients. As shown in Fig. 4, C_D and C_L are parabolic with respect to changing beta, while C_S is linear.

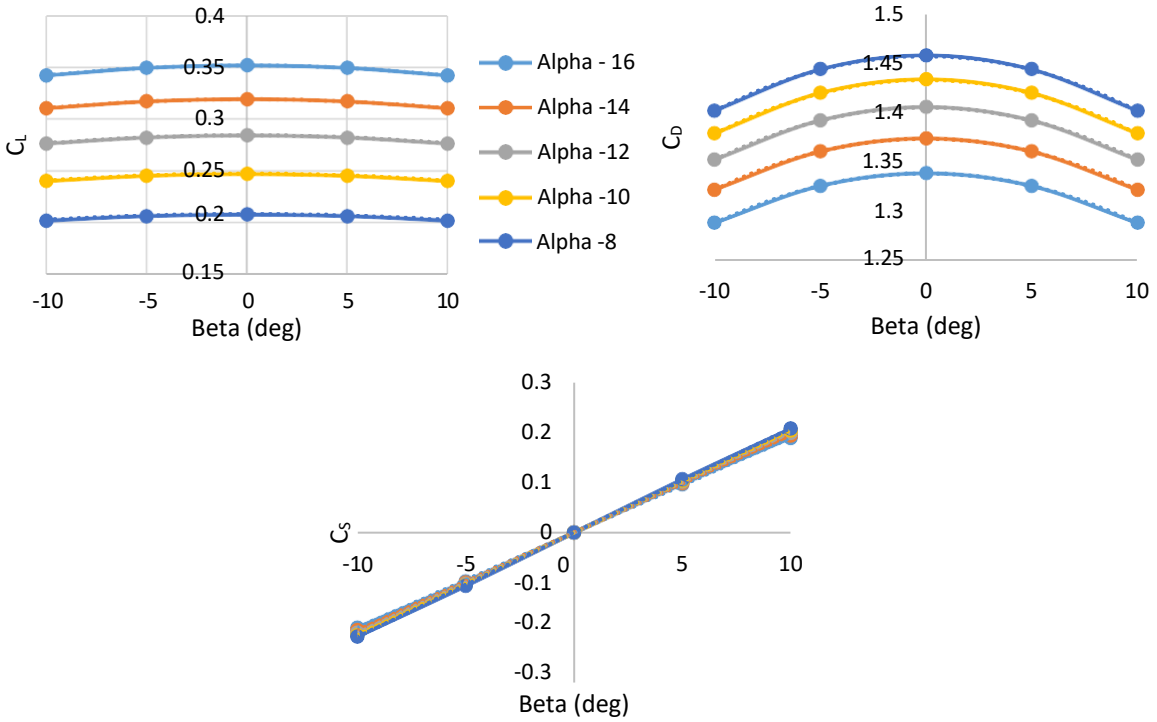

Fig. 4 Lift, Drag, and Side Force Coefficients at Mach 2.

However, each alpha curve may not be a predictable delta from the next as we change in Mach number. To expedite the lookup method used within the predictor corrector, a polynomial fit equation and two-step interpolation method is applied according to Equations 15-17

$$C_{\text{Å,gQn}} = X_{\text{Å}}(M,\alpha)\beta^{?} + Y_{\text{Å}}(M,\alpha)\beta + Z_{\text{Å}}(M,\alpha) \quad (15)$$

$$C_{\text{m,gQn}} = X_{\text{m}}(M,\alpha)\beta^{?} + Y_{\text{m}}(M,\alpha)\beta + Z_{\text{m}}(M,\alpha) \quad (16)$$

$$C_{\text{Ñ,gQn}} = Y_{\text{Ñ}}(M,\alpha)\beta + Z_{\text{Ñ}}(M,\alpha) \quad (17)$$

where each coefficient X, Y, and Z are generated apriori for each vehicle's aerodynamic characteristics.

Another challenge in implementing FNPEG URC stems from developing lateral logic to generate beta commands. To manage crossrange error, FNPEG can find the sign of commanded bank angle by using deadband-based lateral logic similar to Apollo entry guidance, based on the current velocity and crossrange error. Or FNPEG can find the sign of commanded bank with a predictive lateral logic, where the number of desired reversals is input to the simulations and signals a reversal when crossrange reaches the reduction criterion described in Ref. 5. FNPEG URC instead manages crossrange error by using an azimuth-based proportional-derivative (PD) control law defined by

$$\beta_{\text{cnä}} = \frac{\tilde{a}\mathring{a}\c{c}\acute{e}(h\grave{e}Gh)X\c{c}\acute{e}\dot{S}h\grave{e}G\dot{h}\dot{T}\hat{e}G\ddot{e}\hat{n}\hat{n}\ddot{n}\tilde{n}\acute{o}}{\grave{o}\hat{n}\hat{n}\ddot{n}\tilde{n}\acute{o}} \quad (18)$$

where the gains are provided by

$$K_{\text{h}} = \left| \frac{\tilde{N}_{\hat{o}\ddot{o}\tilde{o}\acute{o}}}{c_{\hat{o}\ddot{o}\tilde{o}\acute{o}}} \right| \quad (19)$$

$$K_{\text{h}}^{\cdot} = 2\xi\omega = 2\xi m\acute{u}^{\frac{\c{c}\grave{e}}{n}} \quad (20)$$

Equation 18 is used to calculate the beta corresponding to the side force command, using the same polynomial fit equation from Equation 17. In Equation 21, Γ is shown to be the conversion factor from the side force acceleration to $C_{\text{Ñ}}$

$$\Gamma = \frac{n}{:/?\ \grave{a}\hat{u}} \quad (21)$$

where ϕ is the sensed dynamic pressure and A is the aerodynamic reference area of the vehicle. The azimuth gain is proportional to the maximum side force expected from the maximum allowable beta at the current Mach and alpha combination. While, the azimuth rate gain equation is found based on general relations found from second order linear differential equations. In these equations, ω is the desired augmented frequency and ξ is the desired damping ratio for the system. Despite the fact that the user would need to define the constant, $c_{\ddot{u}\dagger^{\circ}\,\cent}$, to scale with the maximum expected side force and damping ratio, Equations 18-21 provide reliable results with no need for gain tuning across different Entry Interface (EI) to target conditions and only require tuning when changing the vehicle aerodynamics. This is due to the fact that the gains have the capability to automatically increase or decrease in magnitude based on the inherent dynamic pressure reliance of the PD controller.

FNPEG URC incorporated the lateral channel in different manners to increase predictor corrector convergence. First, the algorithm was tested with alpha-only control for a trajectory with zero crossrange error such that the EI planet-relative velocity vector points in the direction of the target latitude & longitude. Once this performed well, the lateral logic was tested within and outside of the predictor corrector loop for trajectories with non-zero crossrange error at EI. While both tests with lateral logic were able to converge, applying the lateral logic within each step of the predictor corrector benefited from stronger convergence rates and better targeting performance without noticeable computation costs. Thus, for all alpha-beta trajectories presented in this paper, the lateral logic is applied within the predictor corrector loop.

IV. Trajectory Design and Design Maps

To increase the applicability of each proposed integrated G&C architecture to future DEV missions, an 11 km/s lunar return demonstration mission was selected to stress the developed technology capability. Lunar returns stress trajectory design by constricting the range of EI flight path angles (FPAs) that could provide satisfactory heating, g-load, and targeting performance. A heat rate constraint of < 250 W/cm^2 was recommended based on the arc jet tests performed with the ADEPT's carbon nanofiber skirt. A g-load constraint of < 15 g's was recommended based on a literature review of other missions carrying sensitive scientific payloads. A targeting constraint of < 3 km was

desirable based on a literature review of the current state-of-the-art guided entry precision targeting expected at Earth and Mars [5, 9]. In order to emulate the non-immediate response of a control system, each FNPEG trajectory has been modeled with a bank rate limit of $15°/s$ and bank acceleration limit of $5°/s^2$. FNPEG URC trajectories were modeled using slower alpha-beta rate limits of $5°/s$ and acceleration limits of $5°/s^2$. These limits were found after performing a rate and acceleration limit study on targeting performance, similar to the methodology used in Ref. 6. Simulation dynamics have been modeled at 100 Hz and guidance is called at a rate of 1 Hz. All trajectories use the Earth Global Reference Atmospheric Model (GRAM) 2010 and an 8x8 Lagrangian gravity field. Each flaps G&C configuration has been modeled with Cart3D aerodynamics, while the others are modeled with CBAERO-Cart3D-anchored aerodynamics.

Once an acceptable EI flight path angle of -5.1° was found using the techniques documented in Ref. 3, a sweep of groundranges to the target were examined to find where the algorithms were sensitive and where the vehicles reached physical limitations. It was found that FNPEG URC shares the same sub-kilometer miss distance performance for similar EI conditions as FNPEG. In fact, Fig. 5 shows a comparison of the tracking for an FNPEG vs. FNPEG URC guided trajectory, and Table 1 shows the inputs used in both guidances. The target site is located at the Utah Testing and Training Range (UTTR) as defined from mission ConOps in Ref. 3.

Table 1. EI and guidance target parameters.

Entry Interface (EI) Parameters	Value	Units
Altitude	122	km
Latitude	-4.7	deg
Longitude	-112	deg
Relative Velocity	11	km/s
Relative Azimuth	0	deg
Relative Flight Path Angle	-5.1	deg

Guidance Target Parameters	Value	Units
Altitude Target	31	km
Latitude Target	40	deg
Longitude Target	-112	deg
Relative Velocity Target	0.69	km/s

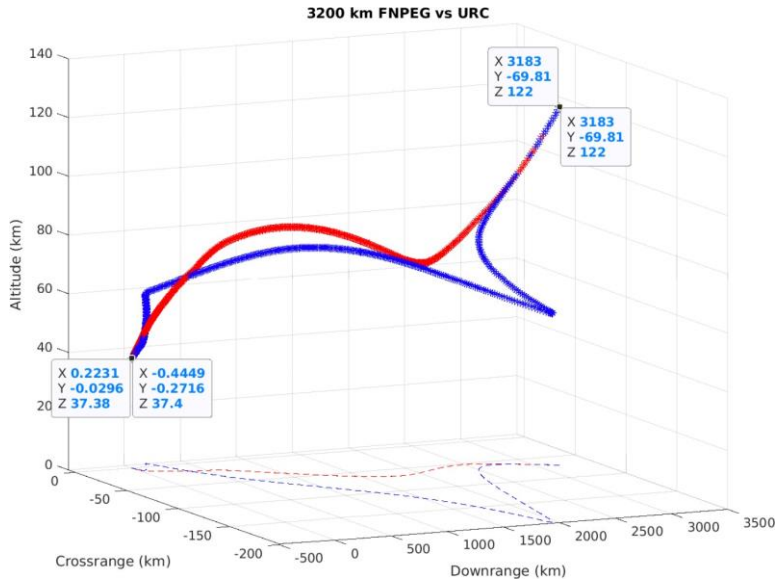

Fig. 5 FNPEG and FNPEG URC trajectory comparison.

As expected, the bank angle trajectory traverses larger crossrange than the alpha-beta trajectory, but both guidances lead the vehicle to within a kilometer of the same target site for descent and landing initiation. In order to find an appropriate EI range to target for each G&C configuration, sweeps of different groundrange to targets were generated by fixing the target latitude and longitude, then varying the EI latitude and longitude. Figures 6 and 7 show the results of range sweep studies done for both bank and alpha-beta profiles. All cases for FNEPG and FNPEG URC begin guidance after a g-load trigger of 0.05 g's has been reached. In these example cases, FNPEG may command bank angles in the range of $\pm 180°$, while FNPEG URC may command angles of attack in the range

of [-18°, -1°] and sideslip angles in the range of ±10°. As expected, if an EI range to target is too small, like in Fig. 6a for the 2,200 km range to target profile, FNPEG URC holds the minimum magnitude alpha command allowable in order to increase drag by pitching the vehicle closer to the geometric centerline at $\alpha = 0°$. This alpha effect on L/D is confirmed in Fig. 6c and would help to avoid overshooting the target if possible. However, if the range to target is very large, like for the 5,000 km range to target profile, FNPEG URC increases the magnitude of the average alpha command. For the four out of five cases that converged on feasible solutions, all increase available lift near the end of the trajectory to avoid overshoot and reserve lifting capability in the case of dispersions. Since this is a very high velocity lunar return trajectory at 11 km/s, the g-load profile, and by association the dynamic pressure profile, in Fig. 6f has two peaks no greater than 6 g's. These results are in agreement from previous Orion FNPEG vs. Pred-Guid comparisons from Ref. 5. Additionally, from the flight path angle corridor defined in Ref. 3, it was shown that for lunar return trajectories with the ballistic coefficients used in these configurations, skip out occurs with flight path angles above -5°, approaching zero, while flight path angles below -7°, approaching more negative angles, yield trajectories that exceed our g-load and heat rate limits. As shown in Fig. 6e, a flight path angle of -5.1° for all tested ranges yield a peak heat rate well below 250 W/cm^2 due to the trajectories' lofted nature. However, this lofting can negatively affect controllability since long periods of a flight with zero g-loads would also mean zero dynamic pressure and zero aerodynamic forces and moments for control in mass movement and flaps configurations.

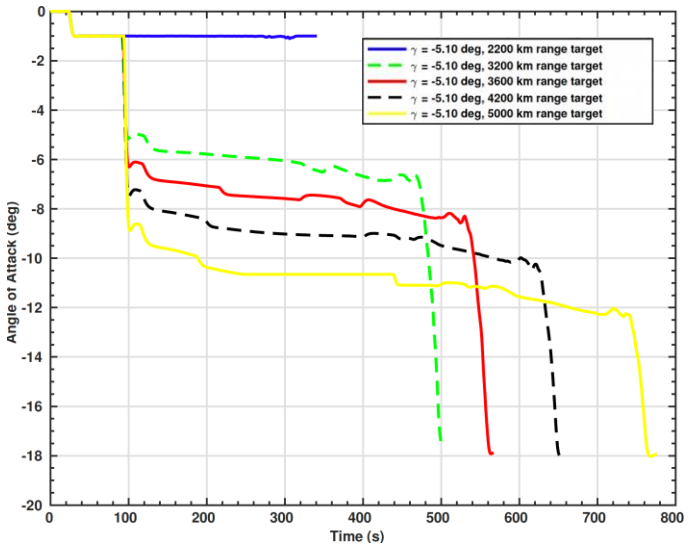

(a)

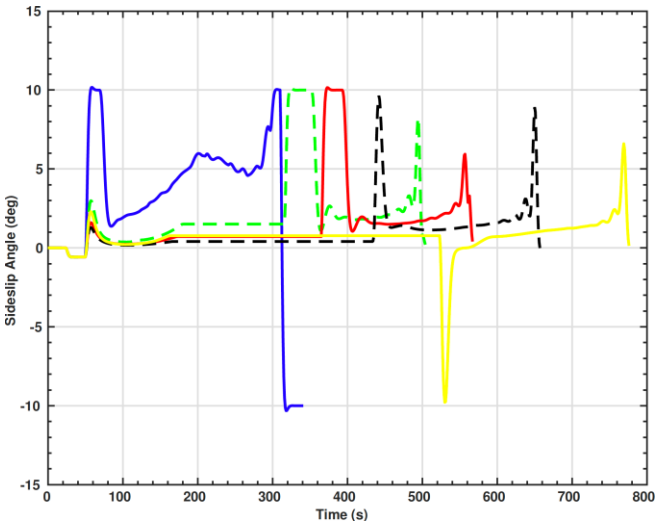

(b)

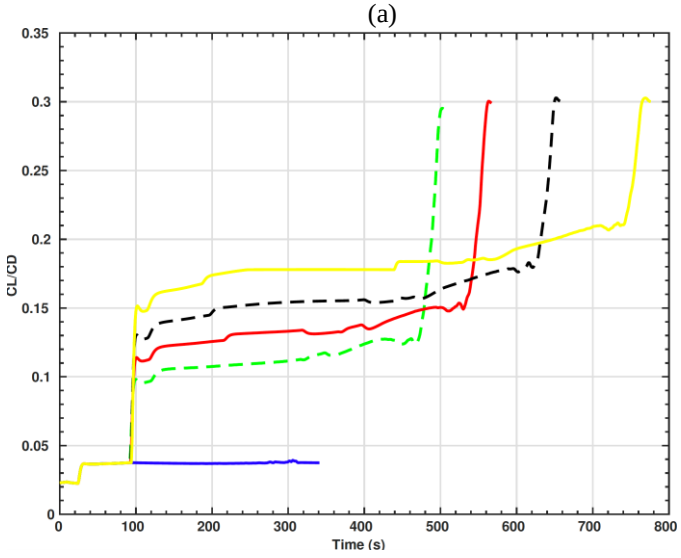

(c)

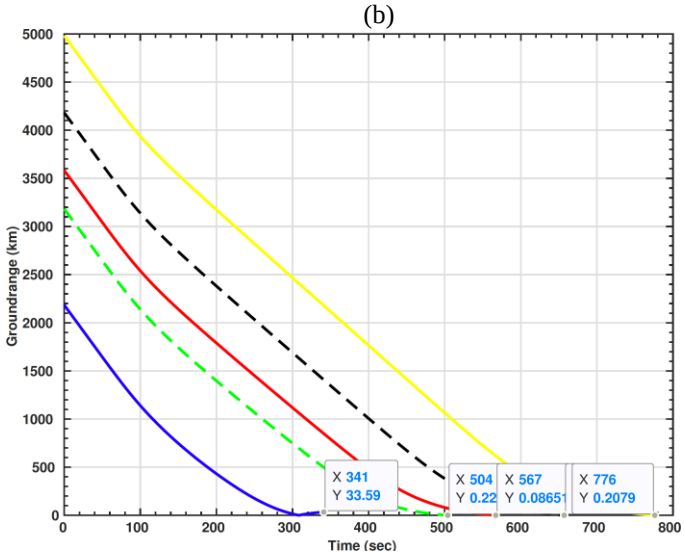

(d)

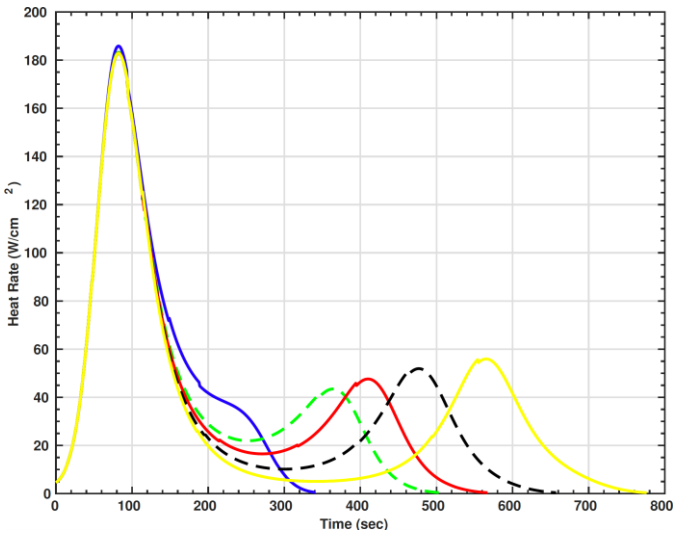

(e)

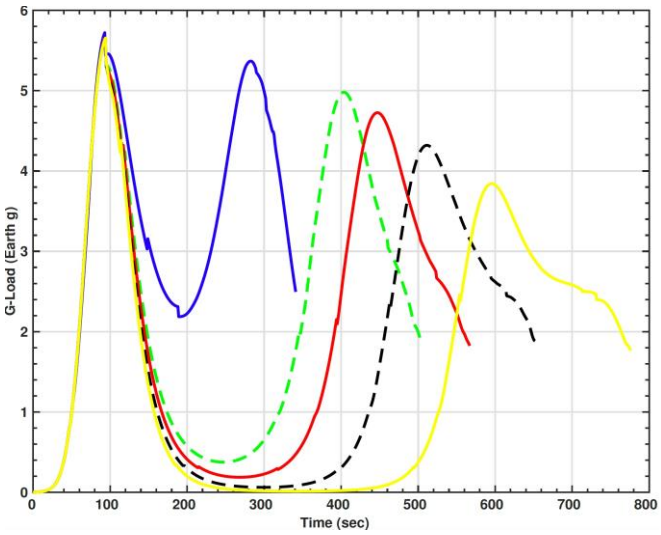

(f)

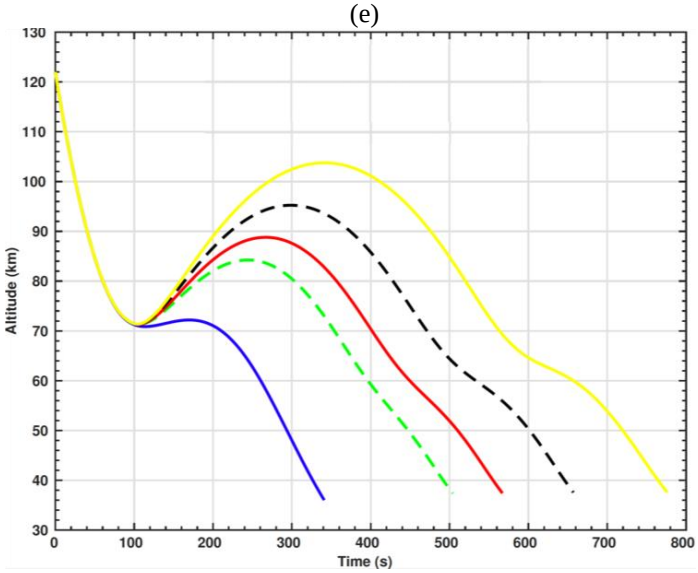

(g)

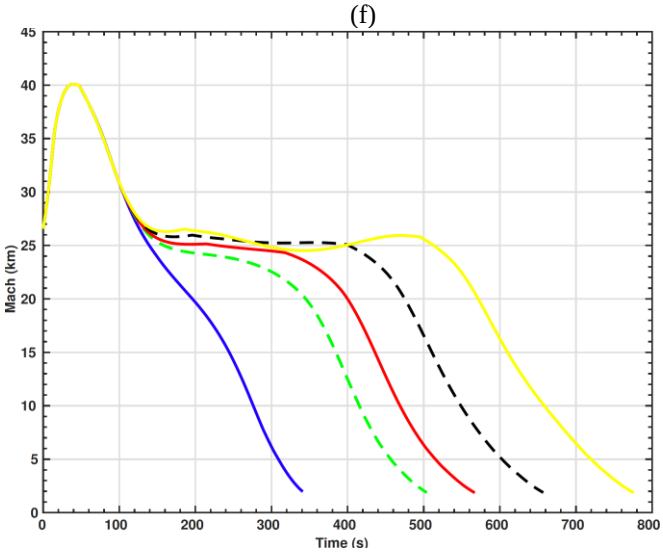

(h)

Fig. 6 FNPEG URC Range Sweep Profiles: (a) Alpha; (b) Beta; (c) Lift-to-Drag ratio; (d) Groundrange; (e) Heat rate; (f) G-load; (g) Altitude; (h) Mach.

Because of this, the lateral logic holds the current sideslip angle command for regimes of low aerodynamic loads below 0.05 g's, then when the loads increase, the vehicle must clean up any errors incurred during the low dynamic pressure regime, as shown in Fig. 6b. Despite these regimes of low controllability, Fig. 6d shows that all cases with feasible range to target inputs reach their targets well within the 3 km limits.

Energy profiles and performance metrics of g-loads, heat rates, and miss distances are very similar between the FNPEG URC and FNPEG profiles. For the smallest range to target profile, the bank angle begins with values closer to 180° than the other trajectories in order to point the lift vector nadir and in the direction of gravity to therefore decrease downrange. FNPEG nor FNEPG URC could reach the target within 3 km for an initial range to target of 2,200 km, but like FNPEG URC, all other cases landed well within 3 km of the target. Due to the full lift-up nature of the alpha-beta trajectories, each range to target has a marginally increased altitude peak as compared to the bank trajectories after the initial descent at EI, but the Mach profiles are nearly identical.

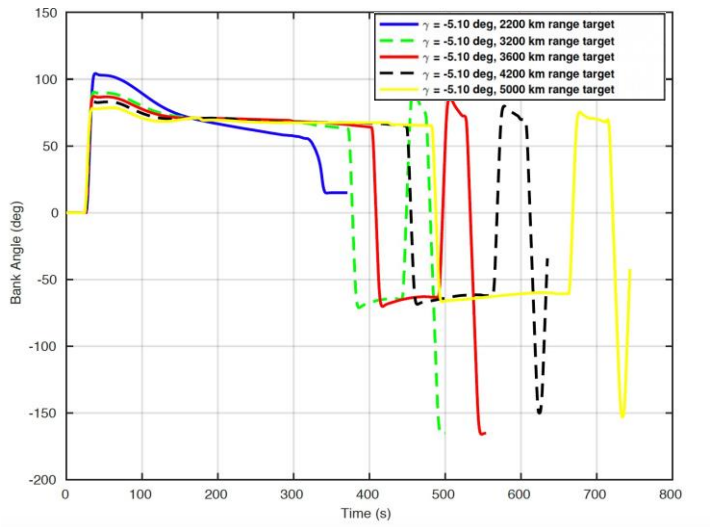

(a)

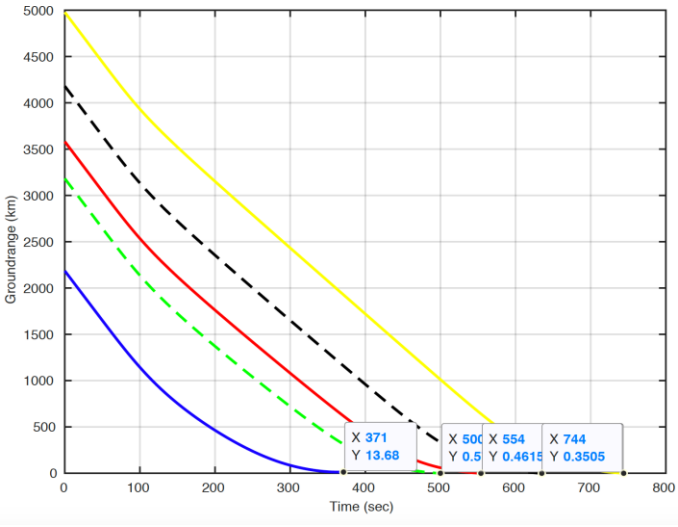

(b)

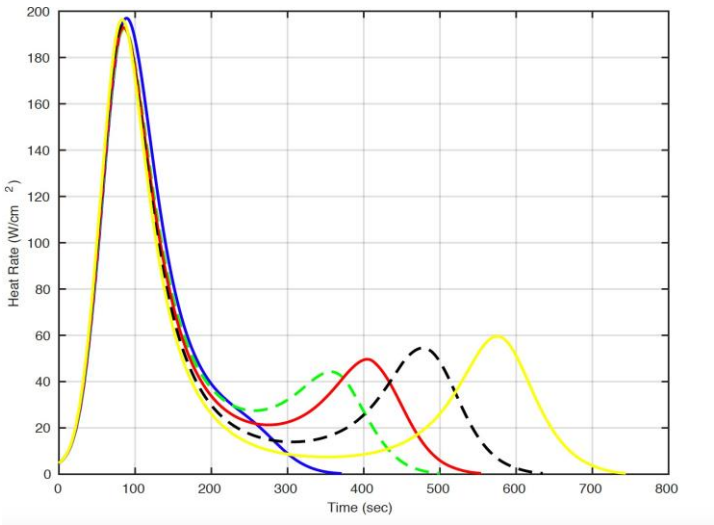

(c)

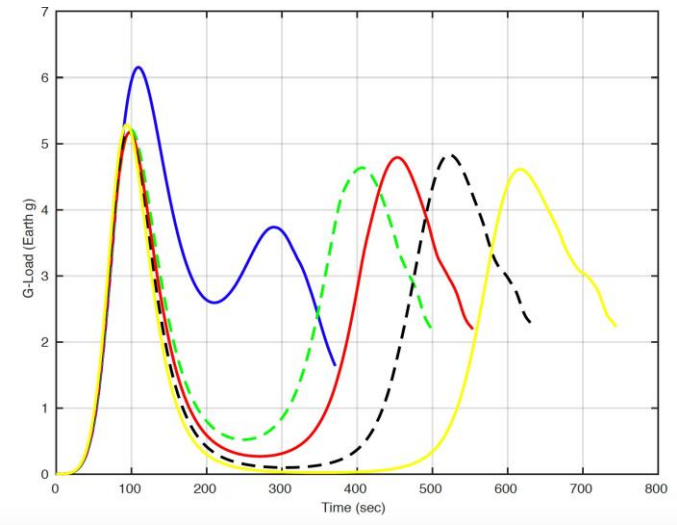

(d)

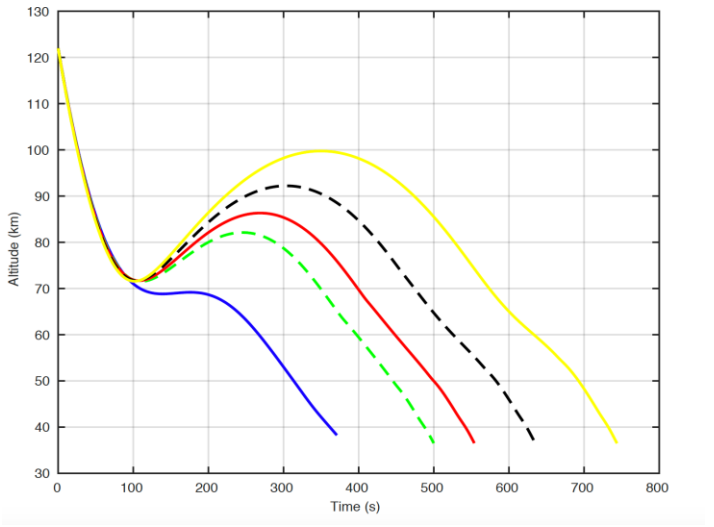

(e)

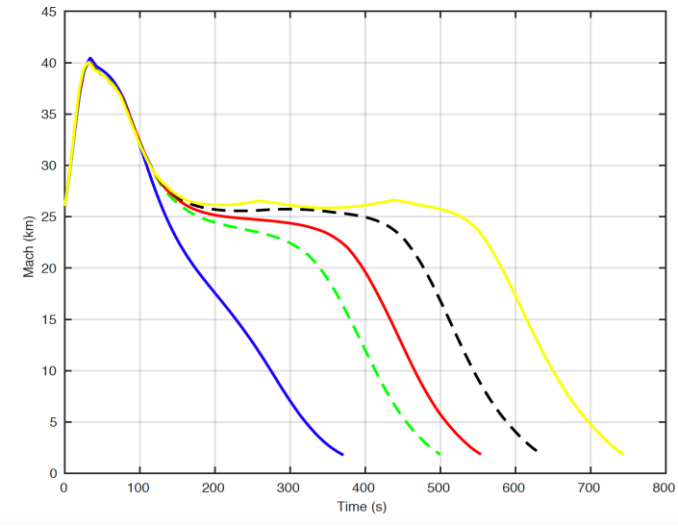

(f)

Fig. 7. FNPEG Range Sweep Profiles: (a) Sigma; (b) Groundrange; (c) Heat rate; (d) G-load; (e) Altitude; (f) Mach.

One of the largest challenges in this study was incorporating the vehicle structural design and control system constraints into the trajectory design process. To promote faster integration, maximum and minimum controllable alphas and betas defined by the aerodynamic stability, structural design, and packaging analysis became inputs into the FNPEG URC guidance. These inputs would restrict the large trade space in the search for a nominal trajectory to only those that comply with the physical limitations of the vehicle and its control system. Due to the large and constrained trade space for each G&C configuration, design maps were employed as an effective tool to explore not only the trajectory design space, but also the vehicle design space.

Trajectory design maps are effective tools at better understanding guidance algorithms as well as any vehicle physics-based limitations. When these have been done for Apollo entry guidance, they have been focused around finding the best changes to improve the performance about a given reference trajectory [9]. However, with the flexibility of no reliance on a reference trajectory, FNPEG and FNPEG URC design maps can explore the effect of a chosen EI state (latitude, longitude, and flight path angle) on performance. Historically, guidances strongly reliant upon reference trajectories (optimized or non-optimized) could have time intensive redesigns, where all coefficients and gain tables would need to be updated and simulations re-run, for mission ConOps updates or changes to vehicle properties. These maps are powerful in giving the trajectory designer an understanding as to how the trajectory could change by preemptively examining the parametric tradespace. In fact, these parametric maps can empower the trajectory designer to never need to apply any heating or load constraints in the guidance to any dispersed cases for carefully chosen nominal trajectories.

FNPEG as well as FNPEG URC were used to produce the design maps for the flaps G&C configuration in Fig. 8 across a wide number of EI to target locations with no gain tuning between simulation runs. Areas in green show trajectories terminating with less than 3 km miss distance, while areas in yellow show trajectories terminating with greater than 3 km miss distance for the targets in Table 1. Considering that the 3-standard deviation uncertainty around a chosen EI point is no larger 0.5° in latitude or longitude, the maps shown in Fig. 8 demonstrate the high flexibility of the algorithms. These maps were created using a computer cluster to run simulations for a modest grid of 45 x 9 EI latitude and longitude inputs. From Fig. 8a-8c, we see that heat rates are not constraining factors for an FPA of -5.1°. However, if we required a higher magnitude flight path angle for this example trajectory, we must ensure our flight path angle is >-6.5° according to Fig. 8c. If mass is later added to a vehicle configuration the ballistic coefficient vs. flight path angle map in Fig. 8d gives insight on how this may impact trajectory design. The red dot shows an example chosen EI latitude and longitude trajectory. The isolines in Fig. 8 can be swapped for any other key performance parameter including peak dynamic pressure, maximum heat load, minimum trough g-load, peak g-load, etc.

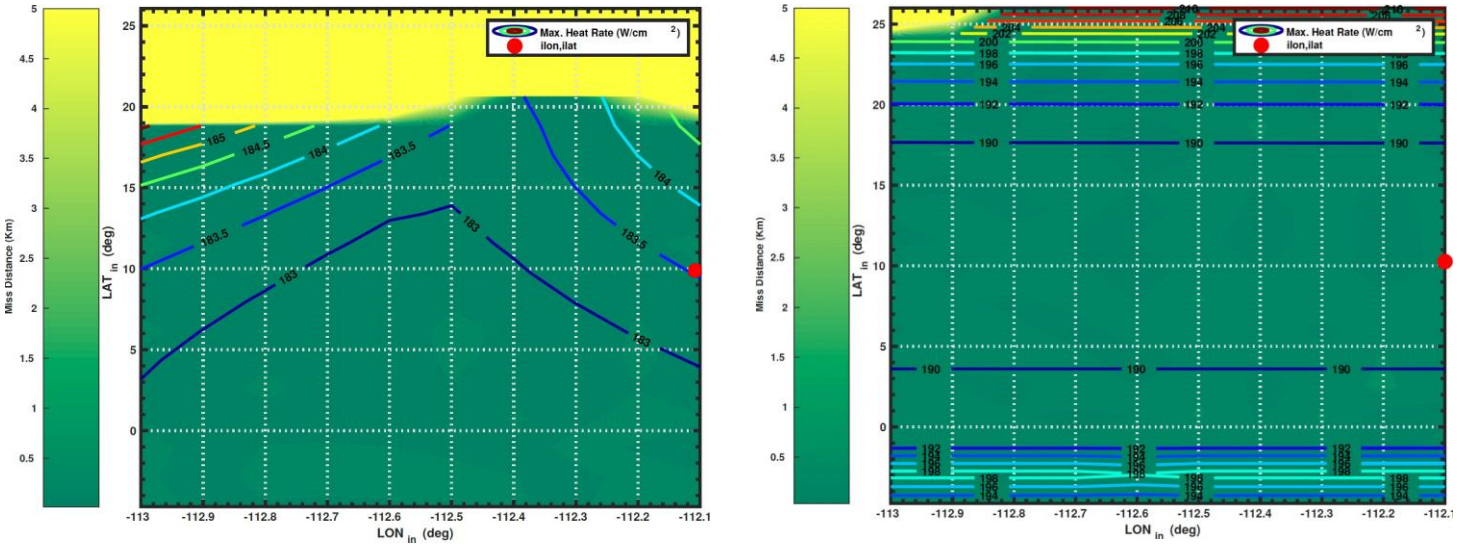

(a) (b)

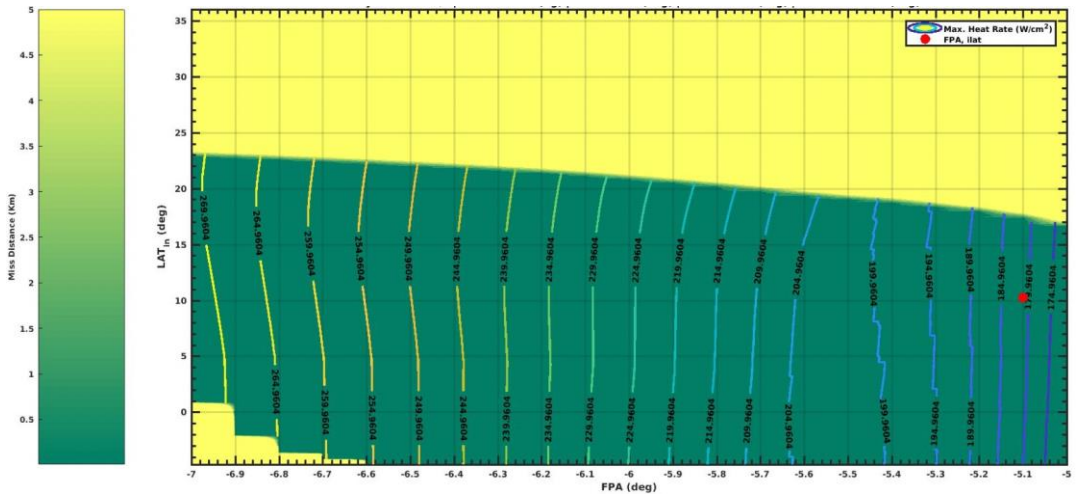

(c)

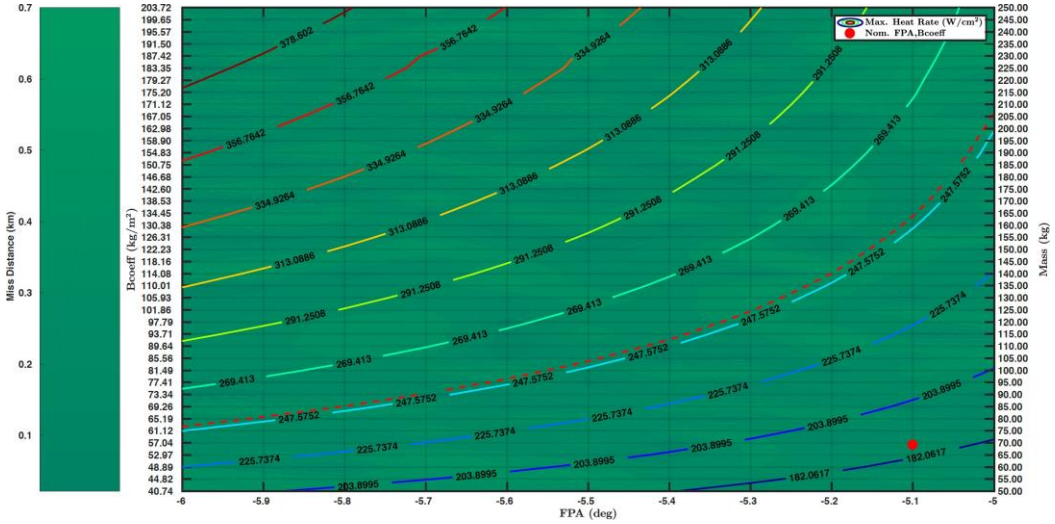

(d)

Fig. 8 Flaps Aerodynamics Trajectory Design Maps for Heat Rate and Miss Distance Dependency: (a) FNPEG URC EI latitude vs. longitude; (b) FNPEG EI latitude vs. longitude; (c) FNPEG EI latitude vs. flight path angle; (d) FNPEG ballistic coefficient vs. flight path angle.

Now, once we start including inputs from the other teams as they iterate, we see in Fig. 9 that our trade space begins to shrink for the flaps alpha-beta G&C configuration. First structural and packaging analysis determined the bounds of alpha bounds about each trim alpha, as shown for flaps version 2 in Table 2. Then the controls team found multiple sets of alpha-beta ranges, that would reduce undesirable roll-yaw coupling based on aerodynamic stability analysis. Based on aerodynamic and structural analyses, the LNA's final version of input alpha ranges for each alpha-beta G&C configuration were all less than zero, yielding positive lift throughout the entire trajectory. In fact, the minimum magnitude of alphas increased with each iteration, limiting the lift reduction capability for each trajectory. While these increases allow for extended range capability, this would inevitably leave longer periods of time with extremely low to no atmospheric density and increase the possibility of skipping out by shifting our usable flight path angle corridor. This is an added challenge for two of the three control system design candidates that rely on aerodynamic forces and moment interactions for control. For flaps version 3, three alpha-beta combinations were defined as controllable and could be chosen for use in the guidance. With the help of trajectory design maps, it became apparent that an alpha-beta range of $[-20.5°, -9.5°]$ was the preferable choice for expanding the trajectory tradespace in finding a nominal trajectory that would likely perform best in a Monte Carlo simulation.

Table 2. G&C configuration constrained allowable alpha-beta ranges.

G&C Design Iterations	L/D Bounds	Alpha Bounds	Beta Bounds
Flaps Version 1	-0.04, 0.33	$+1°, -20°$	$\pm 10°$
Flaps Version 2	0.04, 0.30	$-1°, -18°$	$\pm 10°$
Flaps Version 3a	0.14, 0.33	$-9.5°, -20.5°$	$\pm 0.6°$
Flaps Version 3b	0.20, 0.24	$-12°, -17°$	$\pm 1.0°$
Flaps Version 3c	0.21, 0.23	$-13.5°, -15.4°$	$\pm 1.6°$
Mass Movement Version 1	0.04, 0.30	$-1°, -18°$	$\pm 10°$
Mass Movement Version 2	0.13, 0.24	$-9°, -17°$	$\pm 10°$
Mass Movement Version 3	0.13, 0.24	$-9°, -17°$	$\pm 4.5°$

With increasing L/D minimums, it's shown that for alpha-beta trajectories, the magnitude of the FPA must be increased to find trajectories in this EI latitude vs. longitude trade space that have convergence and avoid skip out. Figures 9 and 10 show that as the alpha and beta bounds input to guidance shrink, so too does the EI tradespace.

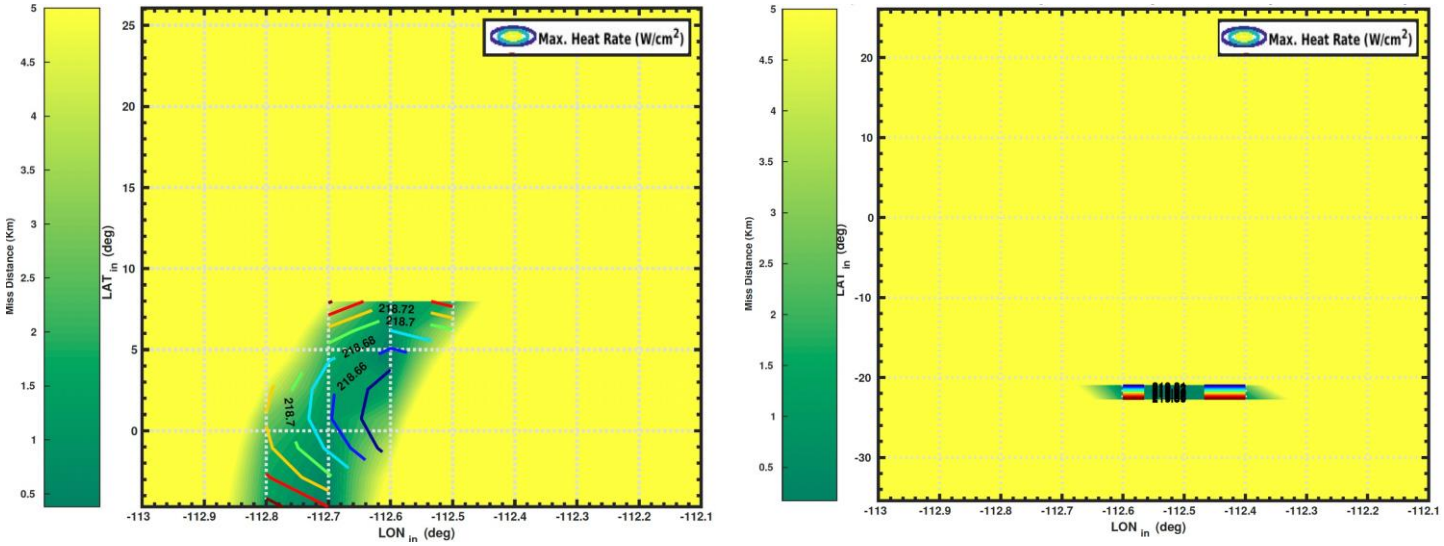

(a) (b)

Fig. 9 Shrinking valid EI tradespace for flaps configuration: a) Flaps version 3a; b) Flaps version 3b.

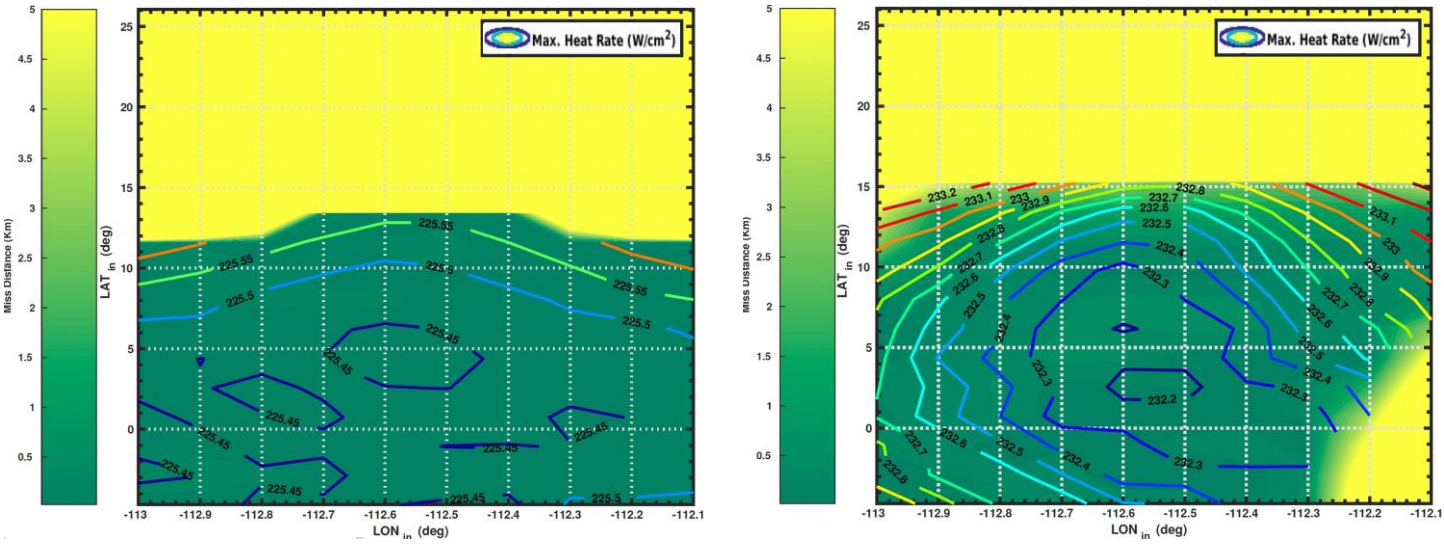

(a) (b)

Fig. 10 Shrinking valid EI tradespace for mass movement configuration: a) Mass movement version 2; b) Mass movement version 3.

Flaps version 3c is not pictured due to the lack of feasible trajectories.

By using the design maps, it became clear that FNPEG URC performance is highly dependent on input alpha and beta ranges. Empirically it was found that an alpha range of at least $\pm 2°$ about alpha trim is needed for good convergence across the explored EI conditions. These maps were also useful in that they became strong indicators of Monte Carlo success, which is useful if running these simulations become expensive on a computer cluster.

V. Dispersed Performance

Monte Carlo simulations are vital in assessing the robustness of a chosen vehicle and mission design. The results of the Monte Carlo simulations became a strong factor in the decision of which G&C configuration is the strongest candidate. Each 1,000 case Monte Carlo was run with the inputs in Table 1 and the dispersions typical for a lunar return trajectory, as shown in Table 3.

Table 3. Monte Carlo inputs.

Monte Carlo Variables	Standard Deviation
Initial Velocity	± 3.33 m/s
Initial Flight path angle	± 0.03 °
Initial Azimuth	$\pm 0.1°$
Initial Latitude	$\pm 0.1°$
Initial Longitude	$\pm 0.1°$
Initial Altitude	± 100 m
Initial Mass	$\pm 1\%$ kg

Monte Carlo Variables	Multiplier
EARTH GRAM iopr	N/A
C_D, C_L, C_S	0.9-1.1

For FNPEG and FNPEG URC, each flight path angle had multiple Monte Carlo simulations that yield mean miss distances well below 3 km, heat rates below 250 W/cm^2, and g-loads below 15 g's. All bank angle G&C configuration trajectories had no difficulty in finding a set of EI inputs that satisfied these limits. To help compare multiple G&C configurations, all shown options in Tables 4-6 use the inputs from Table 1 with the updates of a $-5.2°$ EI flight path angle, an EI longitude of -112.8°, and an EI range to target of 3400 km. Using the RCS G&C configuration trim alpha of $-16.6°$ (L/D of 0.27) and corresponding ballistic coefficient of 54 kg/m^2, we see strong performance. The average miss distance is less than a kilometer, the 99.9%-tile miss distance remains well below 3 km, and the peak heat rate and g-loads are also well below the desired limits. Similarly bank angle guidance maintains strong performance for the mass movement G&C configuration, with a trim alpha of $-13.5°$ (L/D of 0.22) and ballistic coefficient of 64 kg/m^2, and the flaps G&C configuration, with a trim alpha of $-14°$ (L/D of 0.23) and ballistic coefficient of 58 kg/m^2.

Table 4. Monte Carlo results for RCS bank angle guidance configuration (1,000 cases).

Parameter	Mean	99.9%-tile
Miss Distance	0.42 km	0.93 km
Peak Heat Rate	196 W/cm^2	209 W/cm^2
Peak G-load	5.8 g	6.3 g

Table 5. Monte Carlo results for flaps bank angle guidance configuration (1,000 cases).

Parameter	Mean	99.9%-tile
Miss Distance	0.31 km	0.64 km
Peak Heat Rate	198 W/cm^2	211 W/cm^2
Peak G-load	5.7 g	6.2 g

Table 6. Monte Carlo results for the mass movement bank angle guidance configuration (1,000 cases).

Parameter	Mean	99.9%-tile
Miss Distance	0.47 km	1.10 km
Peak Heat Rate	203 W/cm^2	216 W/cm^2
Peak G-load	6.0 g	6.2 g

In order to explore the limitations of the chosen bank angle nominal trajectory, a breakpoint study was performed for the same EI conditions as above, but with lowered L/D capability. This kind of study is useful in the iterative design cycle in informing other teams of how their proposed changes to the vehicle design would start to impact trajectory performance. Table 7 shows that for these EI conditions and a trim alpha of $-10°$ (L/D of 0.17), we begin to see cases undershoot the target due to low L/D and low control authority to overcome severely dispersed cases. Despite the large miss of 27.37 km for the worst case, the average, along with most cases, remain within a kilometer of the target.

Table 7. Monte Carlo results for a nominal trajectory breakpoint study on minimum L/D (1,000 cases).

Parameter	Mean	99.9%-tile
Miss Distance	0.65 km	26.37 km
Peak Heat Rate	193 W/cm^2	207 W/cm^2
Peak G-load	5.6 g	6.2 g

Initial results for the alpha-beta G&C configurations yielded similar strong performance. All trajectories stayed well within the performance parameter limits for the flaps version 2 alpha-beta G&C configuration in Table 8.

Table 8. Monte Carlo results for flaps version 2 alpha-beta guidance configuration (1,000 cases).

Parameter	Mean	99.9%-tile
Miss Distance	0.42 km	0.87 km
Peak Heat Rate	202 W/cm^2	217 W/cm^2
Peak G-load	6.6 g	7.5 g

However, as the team iterated on the vehicle design and completed aerodynamic stability analysis, finding a successful Monte Carlo run became more difficult for alpha-beta guidance configurations. To find the EI latitude, longitude, and flight path angle combinations that would yield the best performance, a Monte Carlo range sweep was performed on each alpha-beta G&C configuration. Minimum altitudes were also checked to ensure that no cases crashed before reaching the FNPEG URC terminal energy. Figure 11 shows an example of these sweeps using the mass movement version 3 configuration with a flight path angle of -5.6° to -5.8°. Flight path angles closer to zero yielded high 99.9%-tile misses due to skip out cases. The EI range to target of 3,613 km for a flight path angle of -5.8° yielded the best statistics, such that the 99.9%-tile statistics only narrowly exceeded 3 km, but the peak heat rates were higher than desired. The same sweep was performed for the flaps alpha-beta G&C configuration in Fig. 12, where no found EI state input yielded a Monte Carlo with miss distances within 3 km for the 99.9%-tile. Results in Table 9 and 10 show the final Monte Carlo results for the alpha-beta configurations. The results in Table 4-6 show that with the given constraints, bank angle trajectories yielded the best performance as compared to the results for alpha-beta configurations. However, for alpha-beta trajectories with larger bounds than given by integrated analysis, we would easily be able to match the FNPEG bank performance.

Table 9. Monte Carlo results for flaps version 3a alpha-beta guidance configuration (1,000 cases).

Parameter	Mean	99.9%-tile
Miss Distance	6.04 km	33 km
Peak Heat Rate	234 W/cm^2	244 W/cm^2
Peak G-load	8.5 g	9.1 g

Table 10. Monte Carlo results for mass movement version 3 alpha-beta guidance configuration (1,000 cases).

Parameter	Mean	99.9%-tile
Miss Distance	0.77 km	3.39 km
Peak Heat Rate	242 W/cm^2	256 W/cm^2
Peak G-load	8.2 g	8.6 g

These results signify that the FNPEG URC algorithm has the capability to give equivalent or better performance to FNPEG, but realistic constraints on the system operational alpha-beta ranges due to yaw roll coupling may reduce the wide applicability of alpha-beta control to lifting low L/D shapes. However, if the alpha trim were closer to the centerline, reducing the minimum alpha magnitude range, both the mass movement and flaps case statistics could improve. Empirically it was also found that an alpha-beta range of at least $\pm 4.5°$ about alpha and beta trim is needed for good Monte Carlo performance. Thus, the recommended configuration would be any FNPEG bank driven G&C configuration, assuming that the control system is able to provide the expected bank rates and bank accelerations used in this study.

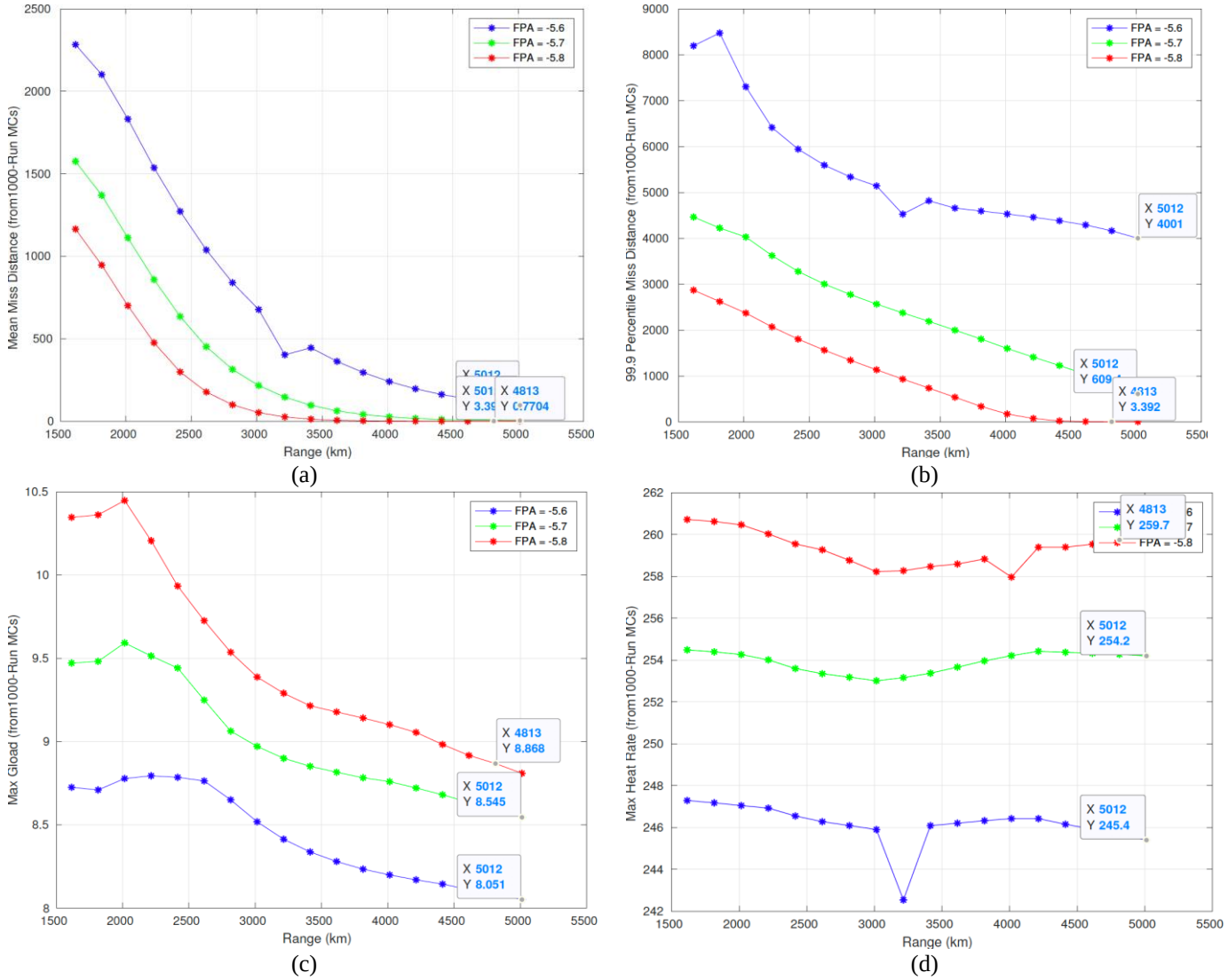

Fig. 11 Monte Carlo range sweep for mass movement alpha-beta configuration: a) Average miss; b) 99.9%-tile miss; c) Peak g-load; d) Peak heat rate.

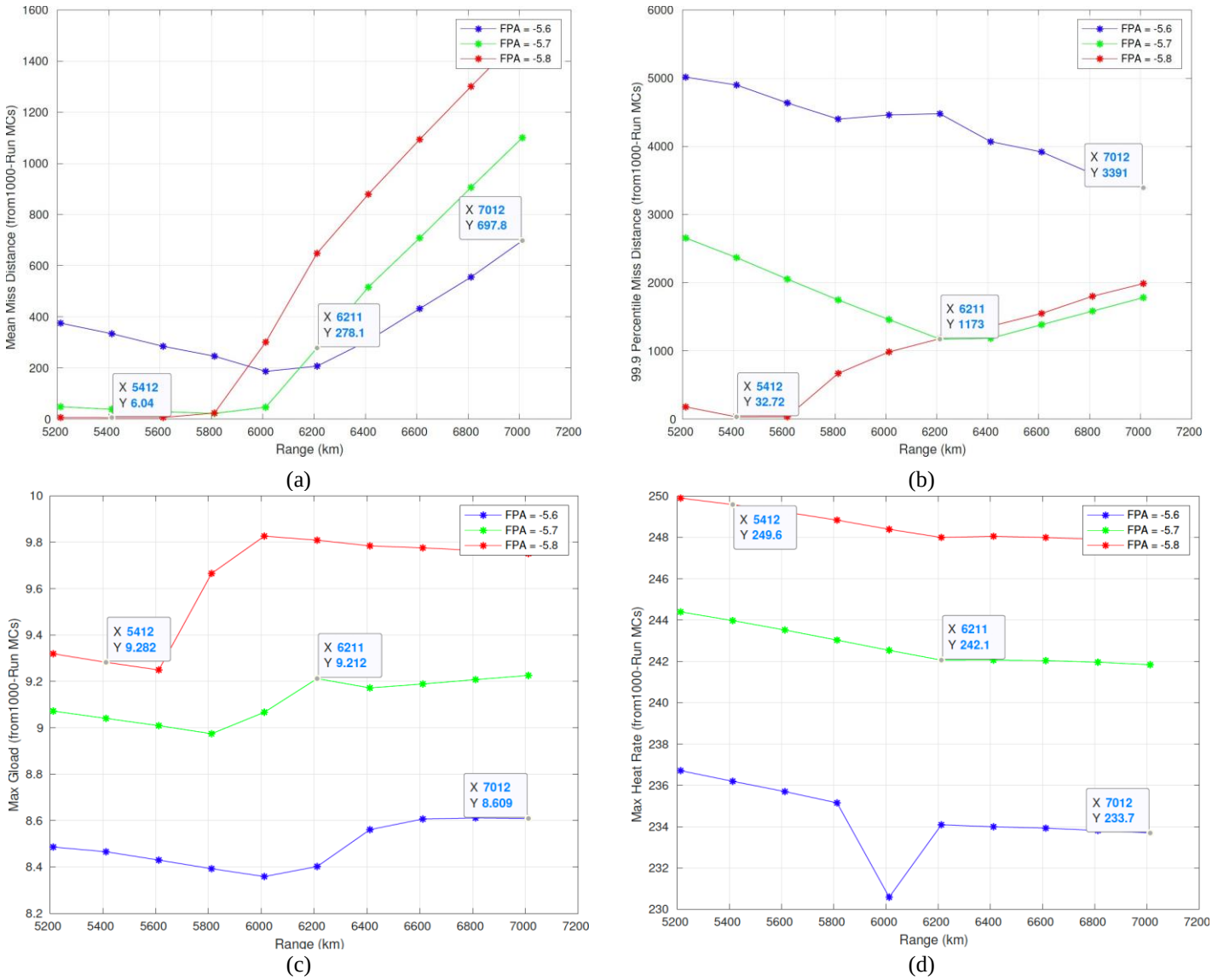

Fig. 12 Monte Carlo range sweep for flaps alpha-beta configuration: a) Average miss; b) 99.9%-tile miss; c) Peak g-load; d) Peak heat rate.

VI. Conclusion

The development and application of the alpha-beta guidance FNPEG with Uncoupled Range Control has been presented. As desired, FNPEG URC yields similar nominal and dispersed performance to the bank angle guidance FNPEG for similar EI conditions. FNPEG and FNPEG URC's unified algorithmic principles allow for a highly flexible trajectory design trade space with little to no tuning across different vehicle ballistic coefficients. Success of FNEPG URC driven designs is strongly dependent on control system and aerodynamic stability analysis driven operational alpha and beta ranges. This study concludes that for vehicles with non-zero trim angle of attack and lift, bank angle guidance may yield a better choice than alpha-beta guidance, especially if integrated system analyses restrict operational beta ranges due to yaw roll coupling. Should alpha-beta guidance be pursued on a vehicle in the future, options should be explored that incorporate both RCS and flaps or RCS and mass movement to alleviate possible areas in the trajectory with little to no dynamic pressure and thus little to no control authority. Even for entry trajectories with less energy than a lunar return mission or entry trajectories with less severe yaw roll coupling, an appropriately sized RCS system would be vital for providing control in highly dispersed cases that incur a roll disturbance that the alpha-beta or bank angle guidance could not control. Nonetheless, there are multiple

configurations presented that can be used to significantly reduce the amount of propellant needed for hypersonic entry by using aerodynamic forces and moments for control.

VII. Acknowledgements

The authors would like to thank NASA Space Technology Mission Directorate's Early Career Initiative (ECI) program for providing the resources to fund this work. Insights from the Pterodactyl team mentor Michelle Munk have been crucial in the direction of this work. The trajectory design team would especially like to thank Ronald Sostaric for his guidance as a mentor throughout the project. We would also like to thank other members of the team that contributed to the work presented including Wendy Okolo, Benjamin Margolis, Brandon Smith, Jason Tran, Alan Cassell, Kenneth Hibbard, and Jeffrey Barton. Further expertise in development was provided by other NASA contributors including Chris Cerimele, Daniel Matz, Jeffrey Bowles, Dave Kinney, and Joseph Garcia.

References

[1] Cassell, A., et al., "ADEPT, A Mechanically Deployable Re-Entry Vehicle System, Enabling Interplanetary CubeSat and Small Satellite Missions," SmallSat 2018, Logan, UT, August 2018.

[2] Cianciolo, A. D., Polsgrove, T. T., "Human Mars Entry, Descent, and Landing Architecture Study Overview," *SPACE 2016*, AIAA 2016-5494.

[3] D'Souza, S., et al., "Developing an Entry Guidance and Control Design Capability Using Flaps for the Lifting Nano ADEPT," 2019 AIAA Aviation a*nd Aeronautics Forum and Exposition*.

[4] Lu, P., "Entry Guidance: A Unified Method," *Journal of Guidance, Control, and Dynamics*, Vol. 37, No. 3, 2014, pp. 713-728.

[5] Lu, P., "Verification of a Fully Numerical Entry Guidance Algorithm," *Journal of Guidance, Control, and Dynamics*, Vol. 40, No. 2, 2017, pp. 230-247.

[6] Johnson, B., Cerimele, C., Stachowiak, S., Sostaric, R., Matz, D., Lu, P., "Mid-Lift-to-Drag Ratio Rigid Vehicle Control System and Simulation for Human Mars Entry," *AIAA SciTech* 2018, Kissimmee, Florida.

[7] Vinh, N. X., Busemann, A., and Culp, R. D., *Hypersonic and Planetary Entry Flight Mechanics*, The University of Michigan Press, Ann Arbor, MI, 1980, Chap. 2.

[8] Brunner, C., and Lu, P., "Skip Entry Trajectory Planning and Guidance," *Journal of Guidance, Control, and Dynamics*, Vol. 31, No. 5, 2008, pp. 1210–1219. doi:10.2514/1.35055

[9] Mendeck, G., Craig, L., "Entry Guidance Design and Postflight Performance for 2011 Mars Science Laboratory Mission," *Journal of Spacecraft and Rockets*, Vol. 51, No. 4, 2014.